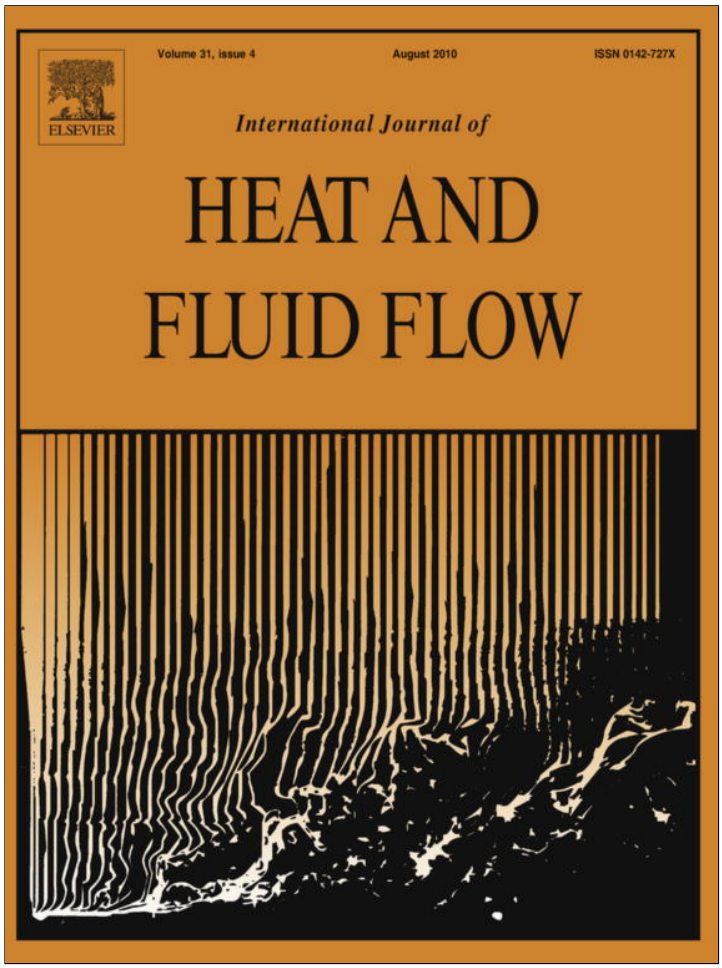

Report Documentation Page

Form Approved
OMB No. 0704-0188

1. REPORT DATE	2. REPORT TYPE	3. DATES COVERED
15 APR 2010		**00-00-2010 to 00-00-2010**

4. TITLE AND SUBTITLE	5a. CONTRACT NUMBER
Transition to turbulence in the separated shear layers of yawed circular cylinders	5b. GRANT NUMBER
	5c. PROGRAM ELEMENT NUMBER
6. AUTHOR(S)	5d. PROJECT NUMBER
	5e. TASK NUMBER
	5f. WORK UNIT NUMBER
7. PERFORMING ORGANIZATION NAME(S) AND ADDRESS(ES) **Naval Undersea Warfare Center,Newport,RI,02842**	8. PERFORMING ORGANIZATION REPORT NUMBER
9. SPONSORING/MONITORING AGENCY NAME(S) AND ADDRESS(ES)	10. SPONSOR/MONITOR'S ACRONYM(S)
	11. SPONSOR/MONITOR'S REPORT NUMBER(S)

12. DISTRIBUTION/AVAILABILITY STATEMENT
Approved for public release; distribution unlimited

13. SUPPLEMENTARY NOTES

14. ABSTRACT
see report

15. SUBJECT TERMS

16. SECURITY CLASSIFICATION OF:			17. LIMITATION OF ABSTRACT	18. NUMBER OF PAGES	19a. NAME OF RESPONSIBLE PERSON
a. REPORT	b. ABSTRACT	c. THIS PAGE			
unclassified	**unclassified**	**unclassified**	**Same as Report (SAR)**	**11**	

International Journal of Heat and Fluid Flow 31 (2010) 489–498

Contents lists available at ScienceDirect

International Journal of Heat and Fluid Flow

journal homepage: www.elsevier.com/locate/ijhff

Transition to turbulence in the separated shear layers of yawed circular cylinders

Stephen A. Jordan

Naval Undersea Warfare Center, Newport, RI 02842, United States

ARTICLE INFO

Article history:
Received 10 November 2009
Received in revised form 15 April 2010
Accepted 20 April 2010
Available online 21 May 2010

Keywords:
Transition to turbulence
Yawed circular cylinders
Separated shear layers
Large-eddy simulation

ABSTRACT

Spatial and temporal resolution of transition to turbulence inside the free-shear layers of two yawed circular cylinders is the subject of the present investigation. These physics were resolved using the large-eddy simulation (LES) methodology. An O-type grid was implemented such that the spatial scales of the LES computation fully resolved the energy range physics of the shear layers at Reynolds number $Re_D = 8000$ based on the cylinder diameter. The two test cases modeled the cylinder span skewed at angles 45° and 60° from the horizontal axis. Observations revealed the same transition process as the normal cross-flow state. Soon after separation, Tollmien–Schlichting disturbances were predicted that evolved into Kelvin–Helmholtz (K–H) eddies before absorption by the large-scale Karman-type vortices. These eddies defaulted to a spanwise wavy pattern similar to a normal cross-flow due to their three-dimensional instability. No mixed modes were found between the K–H (Bloor) and Strouhal frequencies. The effect of yaw angle shortened the transition process. As a result, peak turbulence levels inside the wake formation zone approach the downstream cylinder periphery. In addition, the dimensionless frequencies of the K–H eddies lie above the normal cross-flow relationship as formulated by Bloor (1964). Disparity between the yawed and normal cross-flow states was further emphasized by the shear-layer transition characteristics. Although each property displayed the expected exponential growth during transition to turbulence, their dimensionless form was miss-aligned with those of the normal cross-flow case. Based on the present evidence, additional simulations (and/or experimental measurements) are necessary to form conclusive arguments regarding the expected behavior of the transition characteristics within the free-shear layers of yawed circular cylinders.

Published by Elsevier Inc.

1. Introduction

Understanding transition is paramount to estimating the streamwise formation of large-scale vortical structures in the near wake of bluff bodies such as circular cylinders. Under normal cross-flow conditions, transition to turbulence within the separated shear layers is dependent essentially on Reynolds number where critical defines layers truncated to the turbulent separation point. Below critical, the transition process involves early formation of Tollmien–Schlichting (TS) waves followed by secondary eddies that ultimately mature into the much larger Karman-type structures (see Fig. 1a). This progression is accelerated when the cylinder is oriented at angles of incidence (yaw) to the flow freestream direction. Consequently, the respective time scales of vortex formation are concurrently reduced where zero is reached once the cylinder aligns itself with the freestream. From a Naval systems standpoint involving towed communication cables, arrays, etc., yaw causes a rise in certain flow characteristics such as fluctuating wall pressure that leads to undesirable self and radiated acoustics. Moreover, the cylindrical systems risk operational failure or structural fatigue due to the immediate increase in oscillating lift and drag forces.

Unlike transition, the effect of cylinder yaw on shedding frequency is well-understood via the many experimental and numerical investigations over the past five decades. The earliest works (Hanson, 1966; King, 1977; Smith et al., 1973; Van Atta, 1968) focused on verifying the independence principle where the axial flow characteristics must be decoupled from the concurrent cross-flow components to adequately scale the vortex shedding frequency and base pressure by the normal velocity. For the most part, this principle fails at angles beyond 10° from the cylinder normal axis (Snarski and Jordan, 2001). Contrary to the formation frequency, a definable argument that estimates the vortex shedding angle as a function of cylinder yaw is still at large. While recent studies indicate a sizeable reduction of the shedding angle at large cylinder yaw, others dispute any disparity between the two.

One of the first comprehensive explorations of the transition process from laminar separation to turbulent vortex formation comes from Bloor (1964). Within the cylinder separated shear layers, she hypothesized that transition initiates with the appearance of two-dimensional small-scale instabilities whose streamwise growth amplifies into TS waves. These waves undergo measureable

E-mail address: stephen.jordan@navy.mil

0142-727X/$ - see front matter Published by Elsevier Inc.
doi:10.1016/j.ijheatfluidflow.2010.04.009

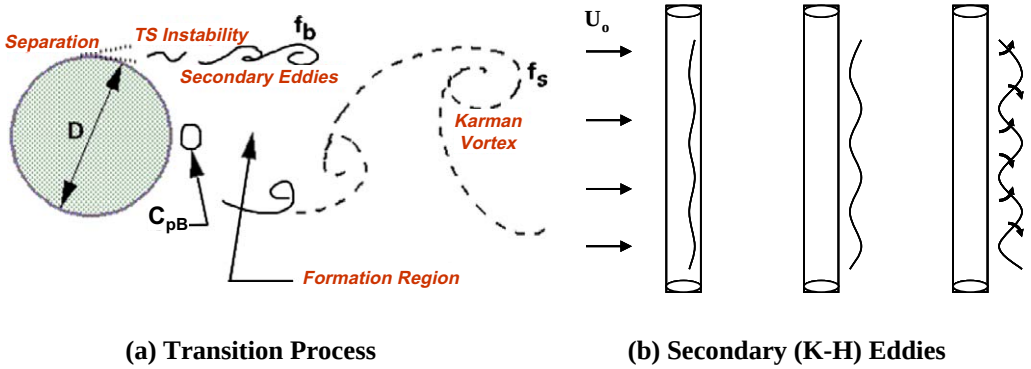

Fig. 1. Transition process to vortex formation of normal flow past a circular cylinder at sub-critical Reynolds numbers.

spanwise distortions that accelerate the transition process. Bloor coined the early disturbances as "transition waves" where her hot-wire anemometer measurements found their streamwise appearance (after separation) to be inversely proportional to the cylinder Reynolds number (Re_D); $Re_D = DU_o/\nu$ where D is the cylinder diameter, U_o is the freestream velocity and ν is the kinematic viscosity. This detection agreed with the earlier measurements by Schiller and Linke (1933) where they noted a drop in the mean transition point $x_{tr}/D = 1.4–0.7$ for $Re_D = 3500–8500$. Bloor also noted unique dependence of the transition-wave frequency (f_b) on Re_D when scaled by the formation frequency (f_s) of the large-scale Karman vortices. She formulated the relationship $(f_b/f_s) \propto Re_D^{\beta}$ given $\beta = 1/2$ for $5000 < Re_D < 25000$. This 1/2 power-law was defended by Bloor under the assumption that f_b scales with the boundary layer thickness at separation. Later, Unal and Rockwell (1988) extended the lower-bound detection of the small-scale disturbances to $Re_D \geqslant 1900$ where their spectral amplitudes varied significantly along the cylinder span.

Wei and Smith (1986) enhanced our physical insight of the transition process to turbulent vortex formation for circular cylinders. Like Bloor, they detected early formation of small-scale TS waves. But their visualization experiments also revealed the creation of Kelvin–Helmholtz (K–H) spanwise eddies whose shear-layer evolution originates from the same instability mechanism described by Bloor. Notably, these eddies have little effect on the downstream base pressure (C_{pB}) inside the formation zone. Beginning with the boundary layer at separation, Wei and Smith reported streamwise transfer of the respective vorticity to the K–H eddies that ultimately was absorbed by the large-scale Karman-type structures. However, this transfer was inconsistent in the spanwise direction which lead to an eventual distortion of the K–H eddies into periodic cellular structures. These structures aligned themselves in the streamwise direction due a reverse feedback mechanism (downstream to upstream) through the shear layers. Wei and Smith further observed breakdown of the cellular appearance into highly irregular structures once the Reynolds number reached the intermediate range (see Fig. 1b).

Besides flow visualization, Wei and Smith (1986) conducted hot-wire anemometer measurements where they reported exponents $\beta = 0.87$ and $\beta = 0.773$, respectively, for the Bloor power-law expression. They reconciled their discrepancy with Bloor's ½-law by scaling f_b with the characteristic momentum thickness along the transition length rather than the boundary layer thickness at laminar separation. Moreover, they revisited Bloor's analogy over a wider range of Reynolds numbers that gave the exponent $\beta = 0.73$. However, Wei and Smith disbelieved the lower-valued exponent based on the premise that the frequency f_b is improperly measured when using anemometry. Prasad and Williamson (1996) compiled their anemometer measurements along with those of Bloor as well as Wei and Smith to obtain the exponent $\beta = 0.6742$ over cylinder Reynolds numbers $1.2 \times 10^3 \leqslant Re_D \leqslant 4.5 \times 10^5$. Their extensive least-square fit provided a convincing argument for defining the scaled transition frequency by the Bloor power-law expression.

Streamwise pairing of the K–H eddies was not visualized by Wei and Smith, nor Unal and Rockwell (1988), in the cylinder free-shear layers. Consequently, the transition frequency f_b does not house sub-harmonics. This characteristic allowed Unal and Rockwell to easily quantify dimensionless flow quantities inside the shear layer segment that owns transition to turbulence. For example, they found an exponential streamwise growth of the dimensionless maximum and edge velocity fluctuations as well as the integrated kinetic energy (see Fig. 2). Moreover, each quantity collapsed onto a single streamwise variation once scaled by their extrapolated values at boundary layer separation. Their growth reaches a plateau once transition completes which disappears at the critical Reynolds number.

Few numerical studies have advanced our physical understanding of the cylinder shear-layer transition process. Braza et al. (1990) computed mixed modes of $nf_s \pm mf_b$ similar to the experimental detections of Kourta et al. (1987), but their excessive integer numbers (n and m) of discrete peaks were directly attributed to their lack of adequately resolving the spanwise physics. Furthermore, they reported streamwise coalescence of the K–H eddies and sub-harmonics that clearly disagreed with the experimental evidence. Jordan (2002) investigated the transition process to turbulence at $Re_D = 8000$ using the large-eddy simulation methodology. By ensuring sufficient spanwise spatial resolution, he properly predicted the Bloor transition-wave frequency f_b including two mixed modes in partial agreement with the spectral measurements of Kourta et al. His computations underscored non-pairing of the K–H eddies and extended the streamwise variations of Unal and Rockwell to a higher Reynolds number.

At present, no comprehensive numerical study has been reported about the transition process to turbulence for the yawed circular cylinder in view of the above free-shear-layer physics. Herein, we aim to begin correcting that deficiency. The present paper examines the structural and quantitative properties of transition inside the separated shear layer at $Re_D = 8000$ and yaw angles $\alpha = 45°$ and $\alpha = 60°$ as measured from the horizontal axis. Like Jordan (2002), the solution methodology is the large-eddy simulation (LES). The fundamental premise of an LES computation is full spatial and temporal resolution of the energy-containing scales of the turbulence motion. The finer scales (beneath the grid resolution) are commonly universal in character and represented by an appropriate sub-grid scale (SGS) model. For the cylinder free-shear layers, the grid-scales must sufficiently capture early generation of the small-scale TS waves and their subsequent local

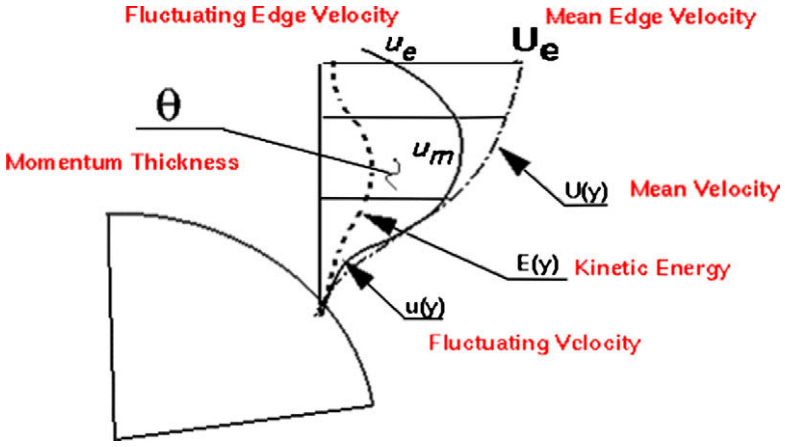

Fig. 2. Characteristic quantities of the cylinder free-shear layer.

streamwise evolution throughout the entire transition cycle. Once resolved, one can ascertain direct correlation between the shear-layer physics of the yawed cylinder to those understood for the normal cross-flow. One should realize however that this study only partially addresses the overwhelming range of possible flow physics that manifest within the separated shear layers over all yaw angles and Reynolds numbers below critical.

2. Resolved field equations

As previously noted, the LES physics comprise the resolved scales by the local grid spacing and un-resolved contributions provided by the SGS model. Resolving generation and growth of the shear-layer TS instabilities, K–H waves and fine-scale physics of the Karman vortex formation requires grid clustering toward the cylinder surface. This stretched structured grid necessitates transforming the Cartesian form of the Navier–Stokes equations into a curvilinear coordinate framework ($\xi^k = \xi, \eta, z$) followed by a mathematical grid filter to acquire the final LES solution set. According to Jordan (1999), this spatial order of coordinate transformation, then mathematical filtering, preserves the commutative property between the differentiation and filter operations. The former transformation operation derives a set of direct numerical simulation (DNS) equations for solution in the computational domain while the subsequent filter operation over uniform curvilinear spacing derives the respective LES formulation. For the yawed cylinder solutions, we will assume that the filter width is synonymous with local grid spacing. The final grid-filtered equations in curvilinear coordinates become

$$\text{Continuity}: \frac{\partial \overline{U}^k}{\partial \xi^k} = 0 \tag{1a}$$

$$\text{Momentum}: \frac{\partial \sqrt{\tilde{g}}\bar{u}_i}{\partial t} + \frac{\partial \overline{U}^k \bar{u}_i}{\partial \xi^k} = \frac{\partial \sqrt{\tilde{g}}\tilde{\xi}^k_{x_j}\bar{p}}{\partial \xi^k} + \frac{\partial \sigma^k_i}{\partial \xi^k} + \frac{1}{\mathrm{Re}}\frac{\partial}{\partial \xi^k}\left[\sqrt{\tilde{g}}\tilde{g}^{k\ell}\frac{\partial \bar{u}_i}{\partial \xi^\ell}\right] \tag{1b}$$

where the two spatial operations redefine the real SGS stress (σ^k_i) in terms of the resolved Cartesian ($\bar{u}, \bar{v}, \bar{w}$) and contravariant ($\overline{U}, \overline{V}, \overline{W}$) velocity components; $\sigma^k_i = \overline{U}^k\bar{u}_i - \overline{U^k u_i}$. Each contravariant velocity component is evaluated in terms of their resolved counterparts using the definition $\overline{U}^k = \sqrt{\tilde{g}}\tilde{\xi}^k_{x_j}\bar{u}_j$. While the overbar in this definition denotes the filter variable, the overtilde symbolizes implicit filtering of the metric coefficients ($\tilde{\xi}^k_{x_j}$) and Jacobian ($\sqrt{\tilde{g}}$) via their numerical approximation.

Temporal evolution of the transition process to turbulence was modeled according to the fractional step method. The convective terms in (1) were spatially approximated by a sixth-order compact stencil in the circumferential ξ and spanwise-periodic z directions with an optimized fifth-order template in the wall-normal η direction (see Jordan, 2007). These terms were time-advanced by the second-order explicit Adams–Bashforth method. All viscous terms (including the SGS model) were approximated by second-order central differences that were time-advance by the implicit Crank–Nicolson scheme to eliminate the associated stability restriction near the no-slip walls. Additional information regarding this solution methodology was presented in detail by Jordan (1999).

3. Dynamic sub-grid-scale model

The turbulent scales removed by the spatial filter operation are termed the sub-grid-scales of the fluid motion. For practical applications, these very fine-scales of turbulence are most commonly represented by the dynamic form of the Smagorinsky eddy viscosity relationship (Smagorinsky, 1963; Lilly, 1992). This form will default to negligible values within the laminar flow regions or turbulence regions of high grid resolution. Furthermore, dynamic evaluation of the SGS model is most important near the cylinder wall segments that bound the upstream side of the vortex formation region. Toward these segments, the turbulent stresses typically display an asymptotic character. After performing the two spatial operations described above for the grid-filtered equations, the dynamic Smagorinsky model for application in the computational space becomes

$$\sigma^k_i - 1/3\tilde{\varsigma}^k_i\tau_{\ell\ell} = 2C\overline{\Delta}^2|\bar{S}|\bar{S}^k_i \tag{2}$$

where the single dynamic coefficient C is evaluated based on the resolved scales. The metric $\tilde{\varsigma}^k_i$ is a grid-filtered term defined as $\tilde{\varsigma}^k_i = \sqrt{\tilde{g}}\tilde{\xi}^k_{x_j}\delta_{ij}$. The turbulent eddy viscosity (ν_T) is defined by the expression

$$\nu_T = C\overline{\Delta}^2|\bar{S}| \tag{3}$$

where $|\bar{S}| = \sqrt{2\bar{S}_{ij}\bar{S}_{ij}}$ and $\overline{\Delta}$ is the grid-filter width. The resolvable strain-rate field ($\bar{S}^k_i$) is expressed as $\bar{S}^k_i = \sqrt{\tilde{g}}\tilde{\xi}^k_{x_j}\bar{S}_{ij}$.

After following the least-squares minimization procedure by Lilly (1992), dynamic evaluation of the SGS model coefficient proceeds according to the expression (Jordan, 2001)

$$C = \frac{L^k_i \cdot M^k_i}{2\overline{\Delta}^2 M^k_m \cdot M^k_m} \tag{4}$$

where the tensor L_i^k is the contravariant form of the modified Leonard term that has the form

$$L_i^k = T_i^k - \overline{\sigma}_i^k \tag{5}$$

The Reynolds stress tensor (T_i^k) becomes $T_i^k = \overline{\overline{U}^k \bar{u}_i} - \overline{\overline{U^k u_i}}$.

The tensor M_i^k is a modeled contravariant stress that is defined in terms of resolvable tensors as

$$M_i^k = \alpha^2 |\overline{\bar{S}}| \overline{\bar{S}}_i^k - \overline{|\bar{S}| \bar{S}_i^k} \tag{6}$$

where the second overbar denotes the test-filter width $\overline{\overline{\Delta}}_t; \overline{\overline{\Delta}}_t = 2\overline{\Delta}_g = \overline{\Delta}$ ($\alpha = 2$).

Unfortunately, explicitly filtering the local instantaneous strain-rates by the test filter in the transformed space can produce negative values for the model coefficient. These contributions were equally seen when test filtering in the physical domain along non-uniform spacing (Jordan, 2001). In the turbulent energy spectrum, positive coefficients denote forward scatter while the negative values symbolize backscatter. Inasmuch as energy backscatter correlates well over long execution times, the negative model contributions can quickly destabilize the LES computation. Thus, all negative coefficients were truncated to zero in the present LES computations to maintain long-term solution stability.

4. Results and discussion

In the following section, we intend to investigate the fundamental physics of transition to turbulence for the yawed circular cylinder at test angles $\alpha = 45°$ and $\alpha = 60°$ as reference to the horizontal axis (see Fig. 3a). More specifically, we desire to discover the initial appearance of TS waves followed by the streamwise maturity of the K–H secondary eddies. These physics are well-known to form within the free-shear layers immediately after laminar separation under normal cross-flow conditions. Both the experimental evidence and numerical predictions have concurred in identifying this process 'a-priori' to the subsequent formation of the downstream turbulent wake at Reynolds numbers below critical. Notably, this particular study is an initial numerical attempt to visualize and quantify the physical impositions on the shear-layer transition process due to a lateral (spanwise) velocity component.

The O-grid generated for this LES application housed $241 \times 141 \times 64$ points in the peripheral (s), normal (r), and spanwise (z) directions, respectively. This grid was utilized for both LES simulations. Equidistant clustering was invoked along the wall-normal direction towards the cylinder surface to insure that $\langle \Delta r^+ \rangle \leqslant 2$ for the first field point throughout the wake formation zone; $\Delta r^+ = \Delta r u_\tau / \nu$, where u_τ is the averaged wall friction velocity computed along the cylinder downstream wall within the formation zone. The wall-normal outer boundary was set at $r_{max} = R = 10D$. Using Kolmorgorov's microscale (η_d) as experimentally measured by Ong and Wallace (1996) and the relationship $\eta_d \sim \mathrm{Re}^{-9/4}$, we can ascertain the adequacy of grid resolution within the free-shear layer region. This resolution is illustrated in Fig. 3b where the profiles depict the dimensionless spatial scales η_d/δ_x and η_d/δ_y along the downstream centerline; δ_x and δ_y are the centerline grid spacing. Knowing that transition completes within $x/D < 1.5$ at this Reynolds number (Jordan, 2002), wave-number cut-off over the region of numerical interest is essentially restricted to the upper bound of the inertial sub-range. In terms of wall units, this spacing translates to $\Delta_s^+ \approx 19$ at $x/D \approx 1.5$ where $\Delta_s^+ = \Delta s u_\tau / \nu$. Thus, the energy scales of the transition process were fully resolved by the present computations. In the spanwise direction, a uniform fine-grid spacing of $\Delta z \approx 0.016\pi$ ($\Delta_z^+ \approx 21$) was implemented to assure capture of the spanwise irregularities. This spacing resolves the spanwise wavelength (λ_z) of the secondary eddies by at least five points (to sixth-order accuracy) according to the experimental measurements by Mansy et al. (1994) and Williamson (1995); $\lambda_z/D \sim 20\mathrm{Re}^{-1/2}$.

External flow conditions involved application of constant streamwise and spanwise velocities (U_∞ and W_∞) on the upstream side of the outer boundary with the contravariant form of Euler's equation (and continuity for closure) along the downstream side; $U_\infty = U_0 \sin(\alpha)$ and $W_\infty = U_0 \cos(\alpha)$. The Euler boundary condition suitably exited the wake structures with no distortions where continuity specifically enforced the incompressibility constraint. The resultant of the constant upstream velocities gave $\mathrm{Re}_D = 8000$ for both yawed cylinders to allow direct comparisons to the normal cross-flow simulations by Jordan (2002) at the same Reynolds number; $U_o = (U_\infty^2 + W_\infty^2)$. Periodic velocity and pressure conditions were enforced along the spanwise boundaries to close the kinematic environment. To expedite the LES computations, both test cases were initialized by the instantaneous variables from Jordan (2002) with appropriate adaptations to the present flow conditions and grid size. A low time step ($\Delta T = 0.001$) was fixed to advance the LES solutions where the statistical evidence was not collected until complete elimination of all flow transients as given by consistent predictions of the mean lift and drag forces.

Before exploring the free-shear-layer physics of the yawed cylinder, we will briefly examine the respective global flow properties of the $\alpha = 45°$ test case in comparison to the experimental and computational data for the normal cross-flow state. Table 1 lists

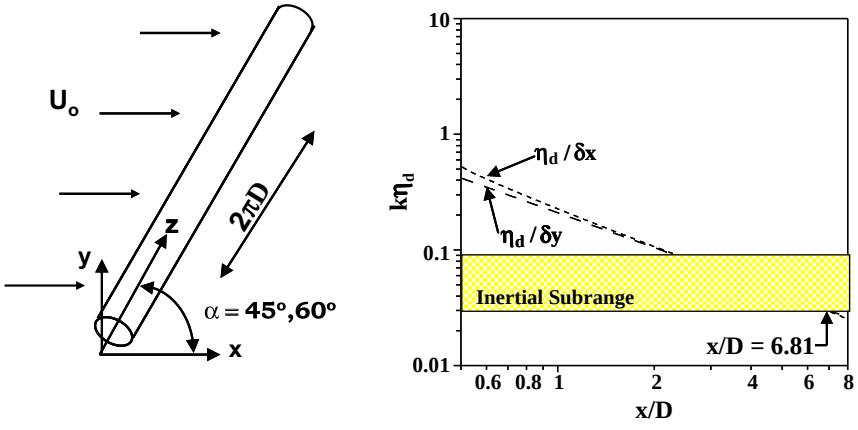

(a) Simulation Conditions (b) Spatial Resolution

Fig. 3. LES Conditions of Yaw, spanwise length and stretched O-grid spatial resolution.

Table 1
Comparison list of several global parameters to the experimental data of normal flow past a circular cylinder (Jordan, 2002) and the present $\phi = 45°$ ($\phi = 90 - \alpha$) yaw angle ($Re_D = 8000$).

Parameter	LES ($\phi = 0°$)	Experiment (0°)	LES ($\phi = 45°$)
C_L (lift coefficient)	±0.115	0.12 (Tadrist et al., 1990)	±0.119
C_D (drag coefficient)	1.06	1.10 (White, 1974)	1.04
S_t (Strouhal number)	0.204	0.205 ± 0.002 (Norberg, 1993)	0.207
u'_p (peak velocity)	0.46	0.45 (Norberg, 1998)	0.49
C_{pB} (base pressure)	−1.08	−1.06 (Williamson, 1995)	−1.02
f_b/f_s (Bloor frequency)	9.4	10.1 ± 1 (Prasad and Williamson, 1996)	11.7
θ_s (separation angle)	92.2	94 ± 2 (Son and Hanratty, 1969)	93.2

the statistical steady-state properties of lift coefficient (C_L), the drag coefficient (C_D), Strouhal number (S_t), peak streamwise fluctuation (u'_p), formation zone base pressure (C_{pB}), scaled Bloor frequency (f_b/f_s) and separation angle (θ_s). Several subtle differences are clearly evident between the normal and yawed cylinders. For example, the coefficient C_{pB} suggests a 6% reduction in base pressure with little reciprocating affect on the resultant drag coefficient. This result should be expected in view of the surface pressure response to a non-zero spanwise velocity component in the yawed cylinder case. Conversely, amplification in the scaled Bloor frequency f_b/f_s is distinctly apparent in Table 1 that suggests earlier formation of the large-scale Karman-type vortices coincident with a larger spatial and temporal decline of the transition cycle. Evidence supporting reduction of the transition time to turbulence is further indicated by a slight increase in the predicted lift coefficient C_L.

While the mean separation angle in Table 1 appears unaffected by cylinder yaw, S_t should vary according to the independence principle with anticipated variations. The LES computations reflect this outcome by predicting a minor increase in the Strouhal number for the $\alpha = 45°$ test case. But a better representation of the shedding behavior is illustrated in Fig. 4 where the Strouhal numbers of both yawed cylinders are scaled by the normal cross-flow values. This figure superimposes the present results as well as previously reported experimental data for $700 \leqslant Re_D \leqslant 1100$ onto the $\cos(\alpha)$ curve. Like the experimental evidence at much lower Re, both LES computations gave Strouhal numbers that deviate above the independence principle.

Given the global properties of the present test cases, we can now focus our attention on the supportive evidence that lie inside the separated shear layers. One of the first concerns of interest is the evolution and spanwise distortion of the K–H structures themselves and their immediate impact on the near-term formation of the Karman-type features. Jordan (2002) did not report large-scale

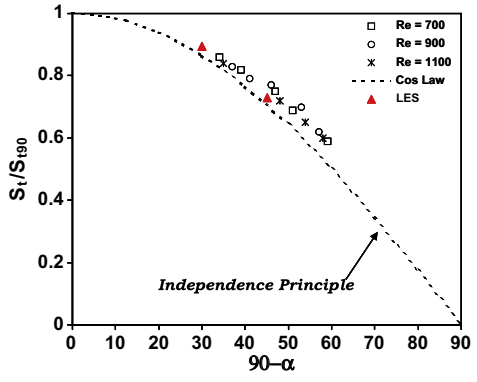

Fig. 4. Comparison of predicted Strouhal numbers ($\alpha = 45°$ and $\alpha = 60°$) to the experimental evidence and independence principle.

spanwise variability of the secondary eddies for the normal cross-flow which agreed with the visualization testing of Wei and Smith (1986) at their higher Reynolds numbers ($Re_D > 3500$). This observation is only partially supported by the present $\alpha = 60°$ simulation. As illustrated by the iso-surfaces ($\lambda = -2$) and vorticity contours in Fig. 5, the K–H eddies are well-organized with a long wavelength distortion ($\lambda_s \approx 3\pi D/4$) that is aligned in the streamwise direction. The parameter λ as used to identify the iso-surface structure, is the second eigenvalue of the strain-rate tensor of the instantaneous turbulent motion. The spanwise wavy pattern of the K–H eddies shown in Fig. 5 agrees with the experimental visualizations reported by Lin (1981). At comparable Reynolds numbers (based on the normal velocity component), Wei and Smith reported these small-scale structures to possess significant irregularity (more turbulent) with intermittent streamwise alignment. One can also see in Fig. 5 that the organized K–H structures impact early stages of vortex roll-up. While these eddies are visibly stretched further downstream, their spanwise variability is mimicked by the initial formation of the larger-scale Karman-type structures. This observation agrees with our basic understanding of the latter stages of transition to turbulence where the Karman vortices receive a majority of their spanwise vorticity from the K–H eddies.

A snapshot of the instantaneous spanwise vorticity that visibly shows the streamwise evolution of the cylinder transition process (Fig. 1a) within the upper separated shear layer is illustrated in Fig. 6 for the LES test case $\alpha = 45°$. Earliest signs of the two-dimensional TS instabilities emerge at streamwise position $x/D \approx 0.26$ as reference to the separation point. Amplification of the TS waves into K–H eddies is plainly visible over range $0.45 \leqslant x/D \leqslant 1.07$ where the upper bound marks the mid-point of a fully matured secondary structure. At this position, this eddy is speeding through the shear layer at streamwise velocity $u/U_0 \approx 0.56$ or $u/U_\infty \approx 0.80$. A second K–H eddy is observable at position $x/D \approx 1.43$ with a higher instantaneous velocity $u/U_0 \approx 0.71$. Ostensibly, this velocity rise is rooted in the adjacent freestream as well as the nearby pull of the Karman vortex formation which together manifests a streamwise increase in separation gap between successive K–H eddies. The final detectable eddy in Fig. 6 owns position quantities $x/D \approx 1.58$, $u/U_0 \approx 0.21$ and $v/U_0 \approx 0.23$. This particular eddy has already been absorbed by the much larger-scale Karman vortex.

A second set of snapshots of the spanwise vorticity through the formation zone and bounding shear layers are shown in Fig. 7 for both test cases. These slices depict vorticity contours where the values in the parenthesis denote their maximums, minimums and increments. The dimensionless streamwise and spanwise velocities ($\hat{u}$, $\hat{w}$) shown over each K–H vortex represent time-averaged quantities over ten transition cycles at the eddy position ($\hat{u} = u_{mean}/U_\infty$). According to these averages, the K–H eddies accelerate in both the streamwise and spanwise directions as well as mature in size; $d\hat{u}/dt|_{60} \approx 0.12$ and $d\hat{u}/dt|_{45} \approx 0.32$. Their streamwise growth in velocity and size agrees in principle with the exper-

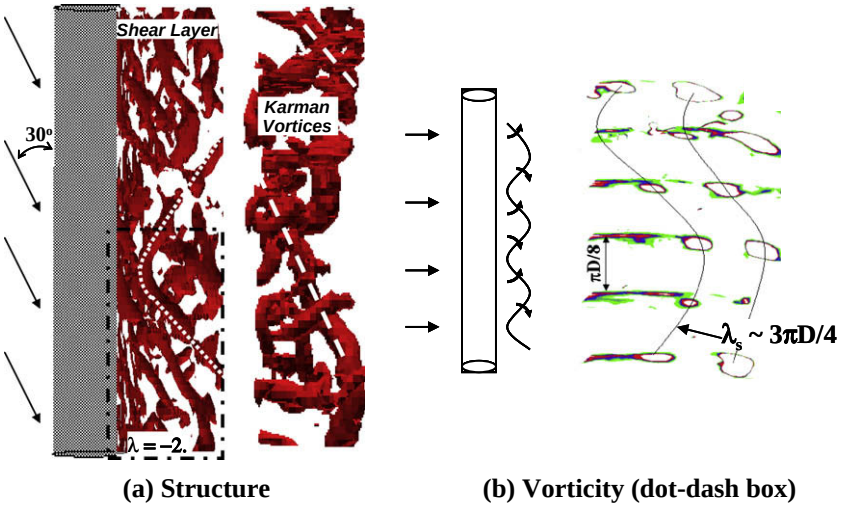

Fig. 5. Spanwise structure ($\lambda = -2$) and vorticity contours (max. 10, min. 0, incr. 0.5) for yawed circular cylinder at $Re_D = 8000$ ($\alpha = 60°$, $\phi = 30°$).

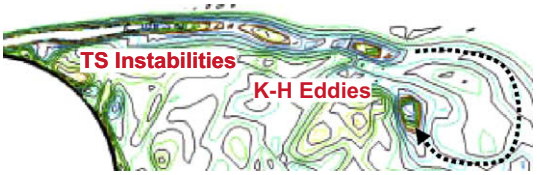

Fig. 6. Snapshot of the spanwise vorticity contours (max.−11, min.−16, incr. 0.5 and max. 25, min. −25, incr. 2.5) showing the TS instabilities and K–H Eddies within the free-shear layer of the yaw circular cylinder ($\alpha = 45°$).

imental measurements made by Unal and Rockwell (1988). In particular, the size variation is attributed to their exponential increase in turbulence levels with downstream distance. A new contribution of the present study is the slight downstream acceleration of the K–H structures in the spanwise direction; $d\hat{w}/dt|_{60} \approx 0.022$ and $d\hat{w}/dt|_{45} \approx 0.017$. Although these levels appear to correlate with yaw angle, they fall well below their relative magnitudes in the streamwise direction.

Besides their spanwise distortion, the streamwise evolution of the K–H structures shown in Fig. 7 is visibly irregular. We note that these two snapshots of the instantaneous shear-layer physics were chosen specifically to reveal this inconsistency. While the left figure ($\alpha = 60°$) suggests an integrated time scale of secondary eddy generation on the order of the Strouhal scaling, the right snapshot ($\alpha = 45°$) clearly indicates their independence. In the former snapshot, one can easily see a premature Karman vortex that has already absorbed smaller-scale K–H eddies of the lower shear-layer. The latter snapshot shows K–H eddies (upper shear layer) stretched and displaced rotationally as they near the larger-scale Karman-type structure. But the final destiny of the lower eddy in the right snapshot is somewhat unclear and its streamwise evolution is an instance of strong asymmetric character. One should note however that these irregular behaviors are sufficiently infrequent such that the upper and lower transition layers share the same statistical evidence.

Another observation in Fig. 7 is the streamwise shortening of secondary eddy spacing with increasing yaw angle; $\Delta x/D|_{45} = 0.43$ and $\Delta x/D|_{60} = 0.40$. Evidence supporting this characteristic is the probability distributions of the streamwise K–H eddy gap ($\Delta x/D$) while passing through the shear layer (see Fig. 8). Mean gap lengths are $\mu = 0.47$ and $\mu = 0.40$ for the $\alpha = 45°$ and $\alpha = 60°$ test cases, respectively, where spacings below these values occur earlier in the transition phase. This gap reduction versus yaw angle should be expected in view of the K–H eddy formation frequency and strength responding to the higher wall vorticity at laminar separation. But several artifacts of yaw angle decline are earlier signs of turbulent transition and vortex roll-up, shortening of the overall formation zone, non-detection of K–H eddy coalescence,

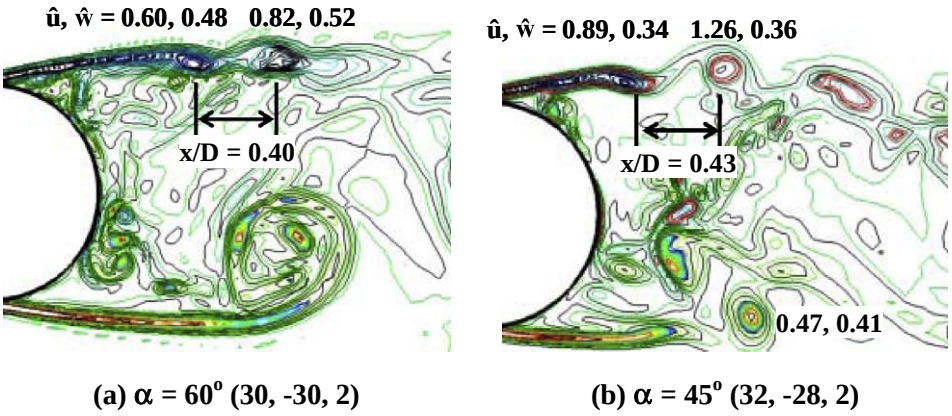

Fig. 7. Snapshots of spanwise vorticity contours (maximum, minimum, increment) highlighting the secondary (K–H) eddies for yawed circular cylinder.

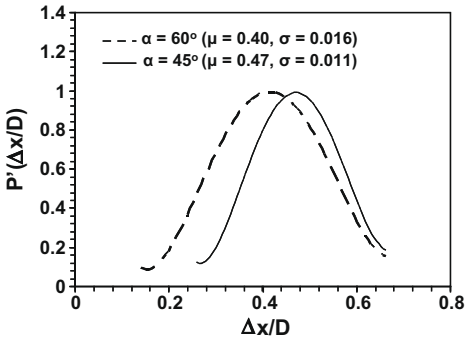

Fig. 8. Probability distributions of K–H eddy gap distances within free-shear layers of two yawed cylinders; $P'(\Delta x/D) = P(\Delta x/D)/P(\Delta x/D)_{max}$.

and closer proximity of the peak velocity fluctuations to the downstream cylinder periphery. Evidence of the latter result is illustrated in Fig. 9 for the streamwise velocity fluctuations ($\langle u'^2\rangle/U_\infty^2$) at yaw angle $\alpha = 45°$ where initial detection of instabilities occurs soon after separation. Interestingly, this turbulent quantity as well as its streamwise length from the mean separation point ($1.38D$) show similar values as the normal cross-flow results when scaled by the normal/freestream velocity ratio (U_∞/U_o). Although not shown, we note that this simple scaling worked equally as well for the $\alpha = 60°$ test case.

Knowing the downstream limits and clear appearance of K–H eddies in the free-shear layers for both test cases involving yawed cylinders, we can now survey the transition process to turbulence from Bloor's perspective. First, we wish to distinguish Bloor's transition-wave frequency (f_b) from the Strouhal shedding cycle (f_s) followed by clear detection of mixed modes on the order $nf_s \pm mf_b$. This approach is illustrated in Fig. 10 by plotting the downstream evolution of streamwise energy spectra (E_{uu}) for the $\alpha = 45°$ test case. These profiles represent spanwise averages over six Strouhal shedding cycles with a 50% overlap (693 total averages). All frequencies and energies are appropriately scaled by the cylinder diameter (D) and the resultant freestream velocity (U_o). The line in each plot denotes the 5/3s slope of the inertial sub-range. Lastly, the relative downstream positions of each profile are given by the successive shear layer cuts in Fig. 10h.

Emergence of the TS instabilities was found in the energy spectra at $x/D = 0.24$ (Fig. 10a) as measured from the mean separation point. This location occurs about 25% earlier than the normal cross-flow case ($x/D = 0.32$). The waves themselves hold dimensionless frequencies near 1 Hz where the spectral peaks below this value are simply harmonics of f_s. Further downstream at position $x/D = 0.33$, the TS instabilities develop into K–H vortices where location $x/D = 0.44$ marks full maturity. The dimensionless Bloor frequency of these eddies attains the distinct value $f_bD/U_o = 1.71$. But further downstream between regions $0.54 \leqslant x/D \leqslant 0.63$, this frequency becomes somewhat broad banded which is contrary to the experimental and numerical evidence for the normal-cross-flow state. Moreover, the energy peaks are comparatively reduced within this range and the expected signs of mixed modes are clearly absent. This latter result suggests that introduction of the velocity component (w), which essentially acts normal to the shear-layer (x–y) plane, prohibits measureable interaction between the K–H and Strouhal vortices. The turbulence matures rapidly within this range that substantially disrupts survivability and coalescence of the K–H eddy structure. Still further downstream at position $x/D = 0.74$ the shear layer forms an inertial sub-range where the small-scale vortices are barely discernible in the respective velocity spectra. Transition has terminated at location $x/D = 0.95$ where the shear layer became fully turbulent according to the energy spectra in Fig. 10f. Interestingly, this downstream limit is 27% shorter than the normal cross-flow computation ($x/D = 1.31$) by Jordan (2002) but confirms the visualization observations ($x/D \approx 1$) by Szepessy (1994).

Recalling the apparent disappearance of mixed modes within the free-shear layer of the yawed cylinder, Fig. 11a shows a sample energy spectra of the $\alpha = 60°$Computation at downstream location $x/D = 0.53$. Again, the dimensionless length is referenced to the mean separation point. Like the previous observations, this sample profile indicates that the spectral peaks below the Bloor frequency ($f_bD/U_o = 1.85$) are harmonics of the Strouhal shedding cycle ($f_sD/U_o = 0.179$). The K–H vortex energy levels are comparatively low and any mixed modes were plainly absent after attempting to find suitable integer values for m and n. As illustrated in Fig. 11b, this latter result may explain why Bloor's frequency scaling does not align with the relationship (f_b/f_s) $\propto Re_D\beta$ for both test cases. The w-velocity component presumably inhibits consistent coupling between the frequencies f_s and f_b that disavows a simple and unique dependence of their ratio on Reynolds number. However, deviation from this frequency scaling appears to correlate well with yaw angle. But additional evidence would be necessary to form a conclusive argument.

As a final look at the shear-layer physics of the yawed cylinder, Fig. 12 shows the downstream distributions of dimensionless integrated kinetic energy (E') and momentum thickness (θ/D) at four selected spanwise planes (z/D) for the $\alpha = 45°$ test case; namely, $z/D = \pi/32$, $\pi/4$, $\pi/2$ and $3\pi/4$. Both distributions are evaluated across the shear layer and represent time averages over 55 cycles of transition to turbulence. Cylinder yaw was recognized in the energy distributions by modifying the original relationship of Unal and Rockwell (1988);

$$E' = \left(\frac{1}{2}\int \frac{(u'^2 + w'^2)(y)}{U_e^2\theta_m}\,dy\right)^{1/2} \tag{7}$$

where (θ_m) is the mean momentum thickness and U_e is the local edge velocity (see Fig. 2). With reference to the shear layer, θ_m is taken at the mid-point between the computed limits of transition. Like the normal cross-flow state, these shear layer properties

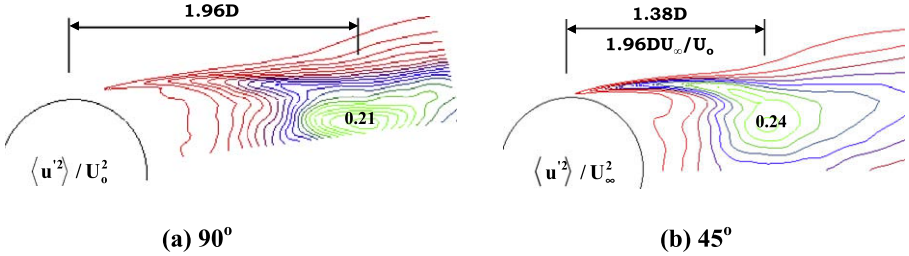

Fig. 9. Contours of scaled streamwise velocity fluctuations for normal (0.21, 0, 0.01) and yawed (0.24, 0, 0.024) cylinders ($Re_D = 8000$); lengths referenced to mean separation point.

display an exponential evolution throughout the transition process. This evolution is clearly consistent but not independent of its spanwise location. Completion of the transition process is readily visible by the abrupt termination of this streamwise growth. Both profiles

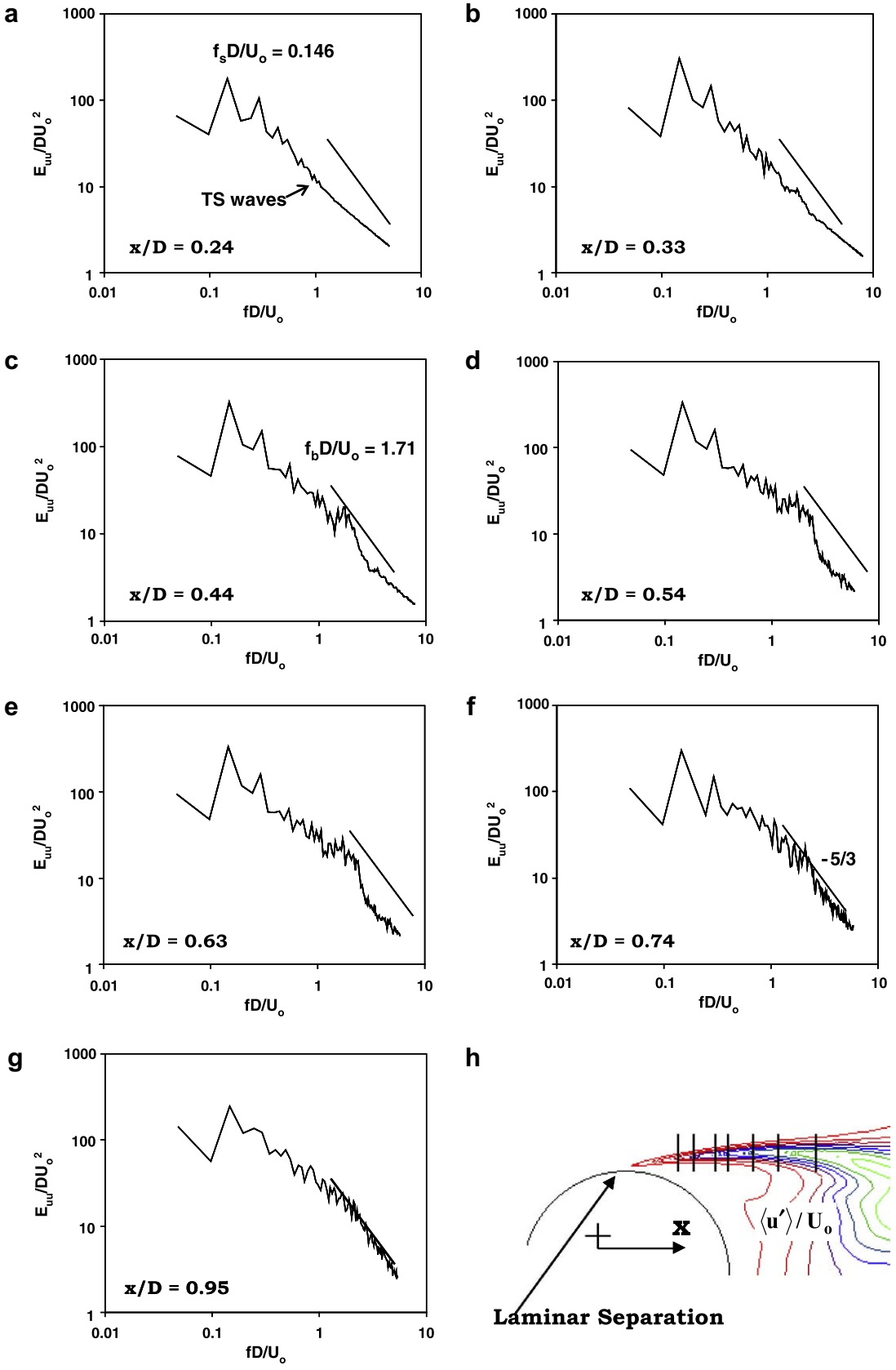

Fig. 10. Scaled spectral energy profiles showing streamwise evolution of the transition process through the cylinder separated shear layer ($\alpha = 45°$).

suggest transition to turbulence concludes at $x/D \approx 0.88$ which coincides with the energy spectra plotted in Fig. 10g. Similar profiles of the $\alpha = 60°$ simulation show that transition ended at $x/D \sim 0.92$.

Given these characteristic distributions, we are now interested in establishing similarity with the normal cross-flow case. Following the earlier work of Unal and Rockwell (1988) and Jordan (2002), both properties are spanwise averaged over the streamwise limits of transition with the resultant distribution of E' subsequently scaled by its pseudo-intercept at $x/D = 0$. Results of this scaling are plotted in Fig. 13a where the characteristic streamwise length over the transition limits was changed to x/θ_m. Only a cursory look is necessary to conclude that the yawed cylinder distributions are plainly dissimilar from the normal cross-flow. The relative slopes suggests that the growth of E' diminishes with yaw angle, but additional test cases would be required to explore a definable association.

On the contrary, the downstream distributions of θ/D coincide for both yawed cylinders as shown in Fig. 13b with similar exponential growth rates as the normal cross-flow. Although intriguing,

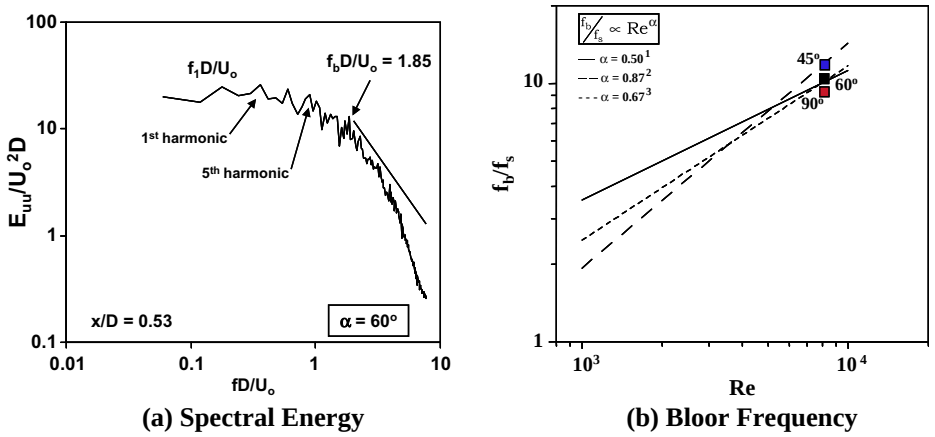

Fig. 11. Profile of scaled streamwise kinetic energy at $x/D = 0.53$ for yaw cylinder ($\alpha = 60°$) and scaled Bloor frequency versus Reynolds number; [1]Bloor (1964), [2]Wei and Smith (1986), [3]Prasad and Williamson (1996).

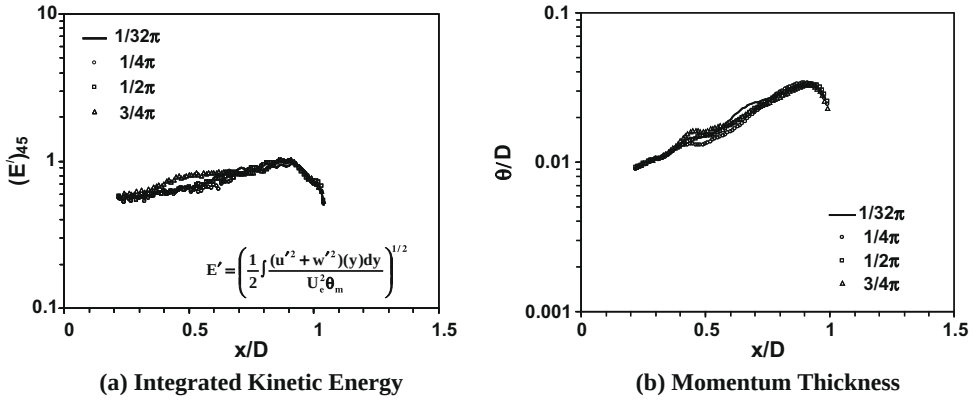

Fig. 12. Streamwise evolution of the integrated kinetic energy and momentum thickness through the separated shear. Layer at four spanwise planes of a yawed cylinder ($\alpha = 45°$).

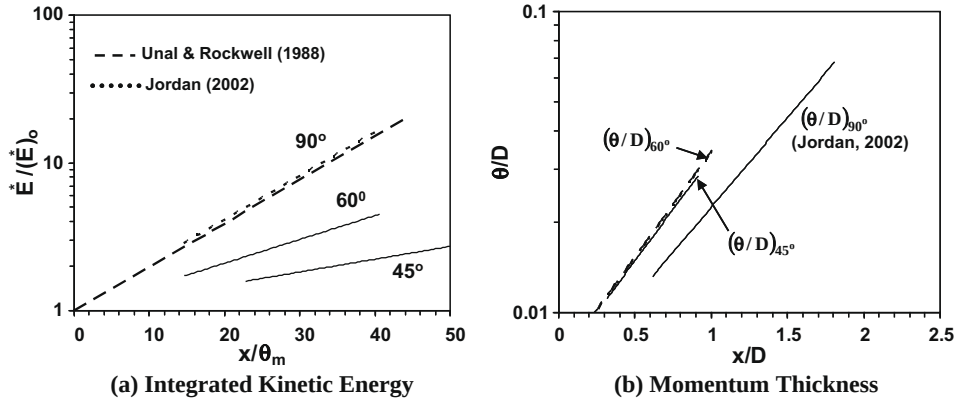

Fig. 13. Streamwise evolution of the integrated kinetic energy and momentum thickness (spanwise averaged) through the separated shear layer.

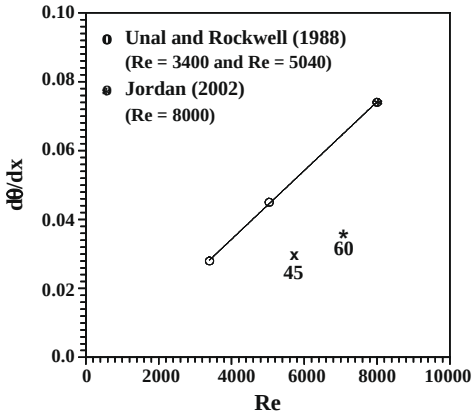

Fig. 14. Mean growth rate of momentum thickness through transition of normal and yawed cylinder (Re based on normal velocity).

this discovery demands further computations (and/or experiments) at varying conditions to attain conclusive proof. This statement is clearly supported in Fig. 14 where the mean growth rate of θ as evaluated through the transition region is plotted versus Reynolds number (Re) based on the normal freestream velocity (U_∞). Both rates deviate substantially from the characteristic curve for the normal cross-flow case over the range of intermediate Reynolds numbers.

5. Final remarks

The present LES computations of transition to turbulence within the separated shear layers of two yawed circular cylinders reveal very interesting results when compared to each other as well as to the normal cross-flow state. At the Reynolds number $Re_D = 8000$ (below critical) and yaw angles $\alpha = 60°$ and $\alpha = 45°$ (as measured from the horizontal axis), transition to turbulence owns the same fundamental characteristics as the normal cross-flow. The transition process initiates with similar appearances of Tollmien–Schlichting (TS) waves soon after laminar separation that rapidly matured into Kelvin–Helmholtz (K–H) vortices before concluding with formation of the large-scale Karman structures. Taken collectively with the previous experimental evidence, one is drawn to strongly argue for this transition process to be a ubiquitous mechanism within the free-shear layers of circular cylinders or bluff bodies in general. This mechanism seems to easily survive cross-flows that act normal to the shear layer. However, a lower-bound of this transition process must exist as the cylinder span approaches alignment with the freestream flow. This lower limit would distinguish a time scale for the Karman vortex formation where the K–H eddies would simply not evolve within the separated shear layer. We saw this omission in the snapshot of the LES computation at $\alpha = 60°$. But a convincing answer to this question would require extensive supplementary evidence.

The characteristic physics within the free-shear layers of the two yawed cylinders followed the same downstream progression as the normal cross-flow condition. The integrated kinetic energies and momentum thicknesses grew exponentially downstream until the free-shear layer became fully turbulent. Distinguishing their spanwise variability from the normal cross-flow case may be an excellent subject for later investigations. But by resembling the spanwise-averaged normal cross-flow progression, these characteristics are excellent omnipresent indicators for defining the spatial limits of transition. Although not shown, the fluctuating properties inside the free-shear layer of these yawed cylinders displayed equivalent trends. But their streamwise growth rates did not align with the normal cross-flow state as was discovered for the integrated kinetic energy and momentum thickness. As mentioned above, further data is necessary to establish tangible behaviors of the free-shear layer properties for the yawed cylinder.

Acknowledgements

The author gratefully acknowledges the support of the Office of Naval Research (Dr. Ronald D. Joslin, Program Officer) and the In-House Laboratory Independent Research Program (Dr. Anthony A. Ruffa, Program Coordinator) at the Naval Undersea Warfare Center Division Newport.

References

Bloor, M.S., 1964. The transition to turbulence in the wake of a circular cylinder. Journal of Fluid Mechanics 19, 290.
Braza, M., Chassaing, P., Minh, H.H., 1990. Prediction of large-scale transition features in the wake of a circular cylinder. Physics of Fluids A 2, 1461–1470.
Hanson, A.R., 1966. Vortex shedding from yawed cylinders. AIAA Journal 4 (4), 738–740.
Jordan, S.A., 1999. A large-eddy simulation methodology in generalized curvilinear coordinates. Journal of Computational Physics 148, 322–340.
Jordan, S.A., 2001. Dynamic subgrid-scale modeling for large-eddy simulations in complex topologies. Journal of Fluids Engineering 123, 619–627.
Jordan, S.A., 2002. Investigation of the cylinder separated shear-layer physics by large-eddy simulation. International Journal of Heat and Fluid Flow 23, 1–12.
Jordan, S.A., 2007. The spatial resolution properties of composite compact finite differencing. Journal of Computational Physics 221, 558–576.
King, R., 1977. Vortex excited oscillations of yawed circular cylinders. Journal of Fluids Engineering 99, 495–502.
Kourta, A., Boisson, H.C., Chassaing, P., Ha Minh, H., 1987. Nonlinear interaction and the transition to turbulence in the wake of a circular cylinder. Journal of Fluid Mechanics 181, 141–161.
Lilly, D.K., 1992. A proposed modification of the Germano subgrid-scale closure method. Physics of Fluids A 4, 633–635.
Lin, S.J., 1981. The Evolution of Streamwise Vorticity in the Free Shear Layer. Ph. D. Thesis, University of California, Berkley.
Mansy, H., Yang, P., Williams, D.R., 1994. Quantitative measurements of three-dimensional structures in the wake of a circular cylinder. Journal of Fluid Mechanics 270, 277–296.
Norberg, C., 1998, LDV-measurements in the near wake of a circular cylinder, ASME Fluids Engineering Division Summer Conference, Paper FEDSM98-5202.
Ong, L., Wallace, J., 1996. The velocity field of the turbulent very near wake of a circular cylinder. Experiments in Fluids 333, 375–402.
Prasad, A., Williamson, C.H.K., 1996. The instability of the separated shear layer from a bluff body. Physics of Fluids 8 (6), 1347–1349.
Schiller, L., Linke, W., 1933. Druck und Reibungswiderstand des Zylinders bei Reynoldsaachen Zahlen 5000 bis 40,000. Z. Flugtech. Motorluft. 24, 193.
Smagorinsky, J., 1963. General circulation experiments with the primitive equations, I. The basic experiment. Monthly Weather Review 91, 99–164.
Smith, R.A., Moon, W.T., Kao, T.W., 1973. Experiments on flow about a yawed circular cylinder. Journal of Basic Engineering, 771–776.
Snarski, S.R., Jordan, S.A., 2001. Fluctuating wall pressure on circular cylinder in cross-flow and the effect of angle of incidence. In: 2001 ASME Fluids Engineering Division Summer Meeting, New Orleans, LA, May 29–June 1, 2001.
Son, J.S., Hanratty, T.J., 1969. Velocity gradients at the wall for flow around a cylinder at Reynolds numbers from 5×10^3 to 10^5. Journal of Fluid Mechanics 35 (Part 2), 353–368.
Szepessy, S., 1994. On the spanwise correlation of vortex shedding from a circular cylinder at high subcritical Reynolds number. Physics of Fluids 6 (7), 2408–2416.
Tadrist, H., Martin, R., Tadrist, L., Seguin, P., 1990. Experimental investigation of fluctuating forces exerted on a cylinder tube (Reynolds numbers from 3000 to 30,000). Physics of Fluids 2 (12), 2176–2182.
Unal, M.F., Rockwell, D., 1988. On vortex formation from a cylinder; Part 1. The initial stability. Journal of Fluid Mechanics 190, 491–512.
Van Atta, C.W., 1968. Experiments on vortex shedding from yawed circular cylinders. AIAA Journal 6 (5), 931–933.
Wei, T., Smith, C.R., 1986. Secondary vortices in the wake of circular cylinders. Journal of Fluid Mechanics 169, 513–533.
White, F., 1974. Viscous Fluid Flow, McGraw-Hill, New York.
Williamson, C.H., 1995. Vortex dynamics in the wake of a cylinder. In: Green, S.L. (Ed.), Fluid Vortices: Fluid Mechanics and Its Application, vol. 30. Kluwer Academic Publishers, pp. 155–234.